

# Asynchronous warming and $\delta^{18}\text{O}$ evolution of deep Atlantic water masses during the last deglaciation

Jiaxu Zhang<sup>a,b,1,2</sup>, Zhengyu Liu<sup>a,b,c</sup>, Esther C. Brady<sup>d</sup>, Delia W. Oppo<sup>e</sup>, Peter U. Clark<sup>f</sup>, Alexandra Jahn<sup>g,h</sup>, Shaun A. Marcott<sup>i</sup> & Keith Lindsay<sup>c</sup>

<sup>a</sup> Center for Climatic Research, University of Wisconsin–Madison, Madison, WI 53706;

<sup>b</sup> Department of Atmospheric and Oceanic Sciences, University of Wisconsin–Madison, Madison, WI 53706;

<sup>c</sup> Atmospheric Science Program, Department of Geography, Ohio State University, Columbus, OH 43210;

<sup>d</sup> Climate and Global Dynamics Division, National Center for Atmospheric Research, Boulder, CO 80307;

<sup>e</sup> Department of Geology and Geophysics, Woods Hole Oceanographic Institution, Woods Hole, MA 02543;

<sup>f</sup> College of Earth, Ocean, and Atmospheric Sciences, Oregon State University, Corvallis, OR 97331;

<sup>g</sup> Department of Atmospheric and Oceanic Sciences, University of Colorado Boulder, Boulder, CO 80309;

<sup>h</sup> Institute of Arctic and Alpine Research, University of Colorado Boulder, Boulder, CO 80309;

<sup>i</sup> Department of Geoscience, University of Wisconsin–Madison, Madison, WI 53706.

<sup>1</sup> Present address: Computational Physics and Methods (CCS-2) and Center for Nonlinear Studies (CNLS), Los Alamos National Laboratory, Los Alamos, NM 87545.

<sup>2</sup> Corresponding author: Jiaxu Zhang, Los Alamos National Laboratory, MS B258, Los Alamos, NM 87545. Tel: (505) 665-4698. E-mail: [jiaxu@lanl.gov](mailto:jiaxu@lanl.gov)

## Supporting Information (SI) Appendix

# Table of Contents

Method S1: POP2 ocean model .....	3
Method S2: Implementation and validation of oxygen isotope module .....	3
Method S3: The LGM spin-up simulation and the deglacial transient simulation (iPOP2-TRACE)...	5
Method S4: The radiocarbon tracer in iPOP2-TRACE .....	6
Method S5: Computing $\delta^{18}\text{O}_c$ from seawater $\delta^{18}\text{O}_w$ and temperature .....	6
Method S6: Other quantitative model-data comparisons for the Atlantic $\delta^{18}\text{O}_c$ .....	7
Method S7: Sensitivity tracers $\delta^{18}\text{O}_w$ -MWF and $\delta^{18}\text{O}_w$ -Hydro .....	9
Method S8: Tracer budget analysis.....	9
Figure S1. ....	11
Figure S2. ....	12
Figure S3. ....	13
Figure S4. ....	14
Figure S5. ....	15
Figure S6. ....	16
Figure S7. ....	17
Figure S8. ....	18
Figure S9. ....	19
Figure S10. ....	20
Figure S11. ....	21
Figure S12. ....	22
Figure S13. ....	23
Figure S14. ....	24
Table S1.....	25
Table S2.....	26
References .....	28

## Method S1: POP2 ocean model

The ocean general circulation model used in this research is the low-resolution version of Parallel Ocean Program version 2 (POP2) (1), which serves as the ocean component of the CESM1 (2). POP2 is a primitive equation level-coordinate global ocean model. The horizontal grid increases from  $0.8^\circ$  latitude on the equator to  $1.85^\circ$  at the poles, although the grid is a uniform  $3.6^\circ$  in longitude. There are 60 vertical levels, with 10 m resolution in the upper 200 m, gradually expanding to 250 m resolution below 3,000 m depth. The tracer transport equations use the Gent-McWilliams parameterization (3) to compute horizontal mixing and use the modified K-profile parameterization (4, 5) to compute vertical mixing. The overflow parameterization of density driven flows and the tidal mixing parameterization of deep vertical mixing were turned off in this study due to changed paleo-oceanographic bathymetries. Further details of the ocean model are described in Danabasoglu et al. (1).

Compared with its previous version POP, the ocean component of CCSM3 (6), POP2 shows significant differences in terms of infrastructure and physics. The number of vertical levels has been increased from 25 levels in POP to 60 levels. The physical processes have been improved to include new parameterizations to represent previously missing physics and to modify existing parameterizations to incorporate new developments (1). The improved physics leads to a better performance in upper layer features, including better current and thermocline structures and smaller biases in the surface and subsurface temperature and salinity fields. Another character of POP2 is that the NADW-AABW boundary seems less sensitive to changes in climate conditions. In CCSM3, the boundary changes from 3,800 m in present day to 2,400 m at the LGM at  $45^\circ$  N (7). In POP2 of CCSM4, the shoaling of the boundary is 600 m between these two climate conditions (8). But some deep ocean biases present in POP still exist in POP2. One significant bias remaining in POP2 is a low ventilation rate, possibly due to shallow mixed layer depths and relatively small area of deep-water formation regions (1).

## Method S2: Implementation and validation of oxygen isotope module

In the oxygen isotope module, the  $\delta^{18}\text{O}_w$  flux is expressed as

$$\begin{aligned} F_\delta &= E(\delta_w - \delta_E) - P(\delta_w - \delta_P) - R(\delta_w - \delta_R) - M(\delta_w - \delta_M) \\ &= (E - P - R - M)\delta_w - (E\delta_E - P\delta_P - R\delta_R - M\delta_M) \end{aligned} \quad (1)$$

where  $\delta_w$  is the isotopic composition of the surface seawater, which is a globally uniform reference value,  $\delta_E$ ,  $\delta_P$ ,  $\delta_R$  and  $\delta_M$  are the isotopic composition of evaporation ( $E$ ), precipitation ( $P$ ), river runoff ( $R$ ), and meltwater from land ice and icebergs ( $M$ ). It is assumed that there is no isotopic flux during sea ice formation and melting, since the isotopic fractionation in these processes is measured small. The computed  $F_\delta$  is used in the vertical mixing term of the surface layer as the tracer boundary condition. The term  $(E - P - R - M)\delta_w$  is the virtual isotopic flux, analogous to the virtual salt flux, representing the diluting effect of the net freshwater flux. The isotopic composition of precipitation ( $\delta_P$ ) used either observational data (for present-day simulations) or model results (for paleo-simulations). The isotopic composition of runoff ( $\delta_R$ ) used the corresponding local  $\delta_P$  value as an approximation. The isotopic composition of evaporation ( $\delta_E$ ) is dynamically computed in the model, represented by a simple linear resistance model approach (9).

The water isotope module was validated in a 4,000-y modern-control simulation (hereafter referred to as iMODspin). iMODspin was forced by the Coordinated Ocean-ice Reference Experiments phase II (CORE-II) interannually varying atmospheric dataset from 1948 to 2007 (10), which had been used to generate a satisfying modern ocean state in POP2 (11) (Fig. 2A). The seawater  $\delta^{18}\text{O}_w$  was initialized at 0‰.  $\delta_P$  and  $\delta_R$  in Eq. 1 used the Global Network of Isotopes in Precipitation (GNIP, accessible at <http://www.iaea.org/water>) observational database that was gridded onto POP2 grid.  $\delta_M$  was set to zero in modern cases.

The global volume-mean  $\delta^{18}\text{O}_w$  by the end of iMODspin reaches 0.050‰, very close to the observational value of 0.059‰ estimated by the gridded GISS-O18 database (12, 13). The annual-mean surface  $\delta^{18}\text{O}_w$  of iMODspin agrees well with GISS-O18 in general (Fig. S1 A and B), showing high values at low latitudes and low values at polar regions. One model-data mismatch is found in the over-enriched tropical and subtropical Atlantic, probably due to an underestimated  $\delta_E$  in iMODspin. Another mismatch is found in the less-depleted Arctic Ocean, likely due to the missed isotopic precipitation in snowfall. Regarding the intermediate and deep ocean, the annual-mean, zonal-mean Atlantic and Pacific  $\delta^{18}\text{O}_w$  are in good agreement with GISS-O18 (Fig. S1 C to F), showing signatures of the three major water masses (NADW, AAIW, and AABW) in the Atlantic and more homogenous values in the Pacific. The good representation of the major Atlantic water masses holds the key to the subsequent paleo-oceanographic simulations. Model tends to underestimate  $\delta^{18}\text{O}_w$  in the deep NA, mostly because of misrepresentation of surface high values in the NADW formation regions in the Nordic Seas. As will be discussed later, this particular bias

does not affect the LGM-to-HS1 period much, because the deep water formation regions shift to the northern North Atlantic between 45 to 60° N (Fig. S12B) during this period.

### Method S3: The LGM spin-up simulation and the deglacial transient simulation (iPOP2-TRACE)

The 4,900-year LGM spin-up of iPOP2 (hereafter referred to as iLGMspin) consisted of 900 y of physical spin-up and 4,000 y of  $\delta^{18}\text{O}$  spin-up. It used the same geometry as in the fully-coupled TRACE21 simulation (14, 15) during the LGM period. A 2,000-y perpetual loop covering the TRACE21 model period of 22–20 ka was constructed as the forcing fields for it. It was initialized from the LGM temperature and salinity climatology of TRACE21, forced with monthly varying fluxes of momentum, heat, and freshwater as well as sea-ice fractions, and subject to a strong restoring of surface temperature and salinity to TRACE21 results. The restoring time was set 10 days for temperature and 30 days for salinity, the latter of which is longer to provide a larger deviation at surface and allow the model to adjust to a reasonably stable state (16). The equilibrated, Eulerian-mean AMOC strength in iLGMspin is 14.3 Sv, slightly higher than that of TRACE21 during the LGM (12.6 Sv). iLGMspin generates colder and saltier Atlantic deep waters than today's, in good agreement with the LGM reconstructions based on pore-fluid measurements (17) (Fig. S2).

With regards to the water isotopic forcing, the isotopic composition in precipitation and runoffs ( $\delta_P$  and  $\delta_R$ ) in Eq. 1 as well as the relative humidity ( $h$ ) and the isotopic composition of marine vapor ( $\delta_a$ ), which were used in the prediction of the isotopic composition in evaporation ( $\delta_E$ ), were taken from an isotope-enabled atmospheric model (isoCAM3) under LGM conditions (18). This isoCAM3 experiment was 50 years in length, with surface ocean  $\delta^{18}\text{O}$  values prescribed as 1.6‰. There was an extra freshwater flux corresponding to the restoring term for salinity introduced to the ocean, and we considered only its diluting effect (no fractionation effect) on the seawater  $\delta^{18}\text{O}_w$  related to this extra flux due to its small volume compared with other fluxes.

iLGMspin was initialized with  $\delta^{18}\text{O}$  at 0‰ and was stopped after 4,000 y, when global volume-mean  $\delta^{18}\text{O}$  reached 1.05‰. The experiment is designed in this way to somewhat represent the glaciation process from the Last Interglacial to the LGM, except that the forcing was fixed at the LGM level instead of changing transiently. It should be noted that, the ocean  $\delta^{18}\text{O}$  has not reached equilibrium by the end of the simulation, which is most likely what had happened at 22

ka. The way that iLGMspin was set up has implications for understanding the post-glacial changes (22–19 ka) observed in deep benthic  $\delta^{18}\text{O}_c$  as discussed in the main text.

iPOP2-TRACE was initialized from the iLGMspin results at Year 4,000 and forced by the same method as in iLGMspin except that the forcing fields were sequential from 22 ka to 13 ka instead of recurrent. The water isotopic forcing scheme followed iLGMspin, except that we used a series of isoCAM3 snapshot experiments during the 22–13 ka period, 50 y in length and roughly 1,000 y apart (18). These isoCAM3 experiments were forced by the same external forcing as for TRACE21, with surface ocean  $\delta^{18}\text{O}$  values prescribed as 1.6‰ at the LGM and reduced following the sea-level changes to 0.5‰ at 6 ka. In this way, the isotopic compositions in hydrological variables ( $\delta_E$ ,  $\delta_P$ , and  $\delta_R$ ) transiently change with time. The meltwater fluxes in iPOP2-TRACE was prescribed in the same way to TRACE21 (Fig. 1A and Table S1).  $\delta_M$  was set to zero before 19 ka, and was set to its characteristic glacial value of  $-31\text{‰}$  (19) in the Northern Hemisphere after 19 ka. In the Southern Hemisphere starting from 14.35 ka,  $\delta_M$  was set to  $-38\text{‰}$ , based on the  $\delta^{18}\text{O}$  values of close-to-shore TALDICE (20) and Taylor Dome (21) ice cores around 14 ka.

#### Method S4: The radiocarbon tracer in iPOP2-TRACE

An abiotic version of carbon isotopes ( $^{12}\text{C}$  and  $^{14}\text{C}$ ) was included in POP2 following the Ocean Carbon Modeling Intercomparison Project protocol (22, 23). This module considers the solubility pump, by which  $\text{CO}_2$  is transferred from air to sea by gas exchange as Dissolved Inorganic Carbon (DIC, defined as  $\text{CO}_2$  plus bicarbonate and carbonate ions), as the major pathway of atmospheric  $\text{CO}_2$  into the ocean. The error by ignoring the biological pump is about 10% (24), because the biological processes affect  $^{14}\text{C}$  and  $^{12}\text{C}$  compounds in the same manner. A detailed description of the implementation and validation of the module can be found in Jahn et al. (23). In iLGMspin, the abiotic  $\Delta^{14}\text{C}$  was initialized from its values of an iPOP2 modern simulation (23) and was spun up for 6000 years for LGM conditions. The atmospheric  $\text{pCO}_2$  was fixed at 185 ppm in iLGMspin, and was ramped up following the reconstruction (25) in iPOP2-TRACE, same as what was used in TRACE21 (Fig. 1A). The atmospheric  $\Delta^{14}\text{C}$  was fixed at 450‰ for iLGMspin, then was gradually decreased following the IntCal09 reconstruction (26) in iPOP2-TRACE.

#### Method S5: Computing $\delta^{18}\text{O}_c$ from seawater $\delta^{18}\text{O}_w$ and temperature

A recently developed quadratic paleotemperature equation (27) based on *Cibicidoides* and *Planulina* species is used to estimate benthic  $\delta^{18}\text{O}_c$  over all seawater temperatures in the model.

$$\delta^{18}\text{O}_{c(\text{PDB})} = (\delta^{18}\text{O}_{w(\text{SMOW})} - 0.27) + 0.0011T^2 - 0.245T + 3.58 \quad (2)$$

where T is the water temperature in °C, and 0.27 is the conversion factor between the PDB standard and the SMOW standard (28). This gives a local temperature contribution to  $\delta^{18}\text{O}_c$  ranging from  $-0.25\text{‰ } ^\circ\text{C}^{-1}$  in cold waters to  $-0.19\text{‰ } ^\circ\text{C}^{-1}$  in warm waters, or  $-0.22\text{‰ } ^\circ\text{C}^{-1}$  over all temperatures if linearly fitted. Many observational studies assume that *Uvigerina* spp.  $\delta^{18}\text{O}_c$  calcify in equilibrium with surrounding seawater (29) and add species-correction factors to  $\delta^{18}\text{O}_c$  measurements of other species (36). When compared with corrected data reported in many publications, model  $\delta^{18}\text{O}_c$  (results of Eq. 2) needs to add 0.64‰ to account for *Cibicidoides* spp. offset (29, 30).

## Method S6: Other quantitative model-data comparisons for the Atlantic $\delta^{18}\text{O}_c$

Four well-dated, high-resolution  $\delta^{18}\text{O}_c$  cores at intermediate depths that extend from the Norwegian Sea to the tropical North Atlantic (Fig. S6 and Table S2) are compared with the model. In general, the model successfully captures the deglacial features of sharp depletions during HS1 and plateaus during the B-A for the three North Atlantic cores. The model yields similar results at the NA87-22 (55.5° N, 2,161 m) (31, 32) and MD95-2037 (37.1° N, 2,156 m) (33, 34) sites, but the record at NA87-22 has a more abrupt depletion near 17.5 ka and barely changes during mid and late HS1, different from the record at MD95-2037 (Fig. S6 B and C). This lack of details in the model may be related to the simplified freshwater forcing over the 50–70° N band and the low-resolution nature of the model. The variable time series at the Norwegian Sea site during the LGM period may be due to local computational instability (Fig. S6A). Both the model and proxy record at the Norwegian Sea site show a sharper depletion during HS1 than other North Atlantic cores, and an enrichment during the B-A instead of a plateau. The reason of this difference is due to the trapping of a low- $^{18}\text{O}$  signal in the Nordic Seas with a reduced AMOC during HS1 and a flushing of the signal into the interior with a recovered AMOC during the B-A.

At the B-A onset, the northern-sourced water formation was reactivated dramatically (14, 15), which is consistent with the sharp evolution of multiple geotracers in both reconstructions and

the model (Fig. 1). There were, however, small changes in the NA middepth  $\delta^{18}\text{O}_c$  cores (Fig. S6). For example, both  $\delta^{18}\text{O}_c$  at NA87-22 and MD95-2037 reached a plateau after the fast HS1 decrease. A decomposition of the simulated  $\delta^{18}\text{O}_c$  clearly shows that both  $\delta^{18}\text{O}_w$  and temperature components contribute to the HS1 decrease, but compensate each other at the B-A onset (Fig. S6 *F* and *G*). When the AMOC recovers and overshoots, the low  $\delta^{18}\text{O}_w$  water brought by the NADW from the surface is compensated by the accompanying surface cooling that is also brought to the depth. After the AMOC overshooting, the two components returned to their pre-B-A condition (with a mild overshooting of  $\delta^{18}\text{O}_w$ ), leading to a small increase of the  $\delta^{18}\text{O}_c$ .

We also made a model-data comparison for a  $\delta^{18}\text{O}_c$  transect near the Brazil Margin in the South Atlantic (35) below 1,000 m (Fig. S7 and Table S2). The model successfully reproduces the Hovmöller diagram of the observed deglacial  $\delta^{18}\text{O}_c$  evolution with respect to both pattern and magnitude. Both the observations and model show that  $\delta^{18}\text{O}_c$  of upper depths (above 2,500 m) started to decrease at 18 ka, but that of lower depths (below 2,500 m) remained unchanged until about 15 ka. Therefore, the upper-depth depletion led the lower-depth depletion by about 3,000 y. Lund et al. (35) attribute the late lower-depth  $\delta^{18}\text{O}_c$  changes to the late onset of the deep water  $\delta^{18}\text{O}_w$  decrease. However, our model shows that the  $\delta^{18}\text{O}_w$  at 28° S decreased with similar magnitudes at each level during HS1 (Fig. 4*E*). Instead, the warming at 28° S was uneven, with much larger warming at upper depths and smaller warming at lower depths (Fig. 4*F*). A heat budget analysis performed at this location (not shown here) suggests that vertical mixing brought the heat at upper levels down, forming an increased vertical temperature gradient.

We further compare the model simulated  $\delta^{18}\text{O}_c$  with four regional benthic  $\delta^{18}\text{O}_c$  stacks in the Atlantic, each with independent radiocarbon age models (36) (Fig. S8*A*). The four regional stacks sampled cores at intermediate (1,000–2,000 m) and deep (below 2,000 m) sites in both the NA and SA. Using definition of the termination onset as the first  $\delta^{18}\text{O}_c$  point that is at least 0.1‰ lighter than the maximum  $\delta^{18}\text{O}_c$  value (36), the model  $\delta^{18}\text{O}_c$  indicates an earlier termination onset age at the intermediate depth than in the deep ocean, which is consistent with what the observed stacks indicate. However, there are two notable differences between the model and the observed stacks. First, the decreases of the intermediate stacks are much greater than those of the deep ones in the model, whereas this difference in magnitude is small in the observations. Second, the model identifies a later termination onset and a smaller decrease during HS1 in the deep SA stack than in the deep NA, which is not found in the observations. Some of the chronologic differences may

reflect assumptions used in constructing the radiocarbon age models of the stacks, particularly the assumption of a constant reservoir age as well as an averaged age for each region (Fig. S8B).

## Method S7: Sensitivity tracers $\delta^{18}\text{O}_w\text{-MWF}$ and $\delta^{18}\text{O}_w\text{-Hydro}$

The four  $\delta^{18}\text{O}$  surface flux terms in Eq. 1 (besides virtual flux) can be grouped into two categories; meltwater forcing ( $M$ ), which is also known as the volume effect, and hydrographic forcing, which comprises the remaining three terms. To explore the relative contributions of the two categories during the early deglaciation (19–16 ka), we implemented two sensitivity tracers in iPOP2-TRACE. One was  $\delta^{18}\text{O}_w\text{-MWF}$ , which followed the transient meltwater forcing, but its hydrographic forcing was kept as in 19 ka. The other was  $\delta^{18}\text{O}_w\text{-Hydro}$ , which followed the transient hydrographic forcing with no meltwater forcing.

The evolution of  $\delta^{18}\text{O}_w\text{-MWF}$  indicates that the volume effect is the major cause of the  $\delta^{18}\text{O}_w$  depletion at both core locations, and itself would result in a greater magnitude and a mild lead of the depletion of the northern core (Fig. S10B). However,  $\delta^{18}\text{O}_w\text{-Hydro}$  indicates the hydrographic forcing causes an enrichment of the northern core and does not impact the southern core much, therefore opposing the volume effect (Fig. S10C). The relative contributions can be seen clearly in the Atlantic zonal mean changes of the two sensitivity tracers. The  $\delta^{18}\text{O}_w\text{-MWF}$  highly represents the pattern of  $\delta^{18}\text{O}_w$  changes, but with a slight greater magnitude (Fig. S11B). The  $\delta^{18}\text{O}_w\text{-Hydro}$  exhibits enrichment over the whole basin with greatest magnitude at 0–30° N near surface (Fig. S11C), because of a small isotopic fractionation factor (liquid to vapor) in evaporation at warmer temperatures.

## Method S8: Tracer budget analysis

The tracer budget analyses for deep-sea  $\delta^{18}\text{O}_w$  and temperature are based on the tracer transport equation

$$\frac{\partial \varphi}{\partial t} = -u \frac{\partial \varphi}{\partial x} - v \frac{\partial \varphi}{\partial y} - w \frac{\partial \varphi}{\partial z} + \delta_z(\kappa \delta_z \varphi) + M_H(\varphi) \quad (3)$$

where  $\varphi$  represents  $\delta^{18}\text{O}_w$  or temperature. The tracer tendency ( $\partial \varphi / \partial t$ ) is influenced by five terms, from left to right, zonal advection, meridional advection, vertical advection, vertical mixing, and horizontal mixing. The three advection terms are mean advectives (green, purple, and blue curves in the lower panel of Fig. 5), which represent the advective fluxes due to the resolved mean flow.

In the offline diagnosis, they are estimated by a second-order centered discretization form based on the mean velocity ( $u$ ,  $v$ , and  $w$ ) (37). The vertical mixing (brown curves in Fig. 5) in the model represents diapycnal diffusion, and uses the modified K-profile parameterization (4, 5). In the offline diagnosis, it is estimated by a finite-difference discretization form based on  $\kappa$ , which is the vertical diffusion coefficient and is spatially variant. Horizontal mixing (Fig. 5, red curves) in the model uses the Gent-McWilliams parameterization (3), which includes along-isopycnal diffusion and eddy-induced advection. Since this term is not a standard output and there is no offline scheme to directly estimate it, we use the residual term to represent the horizontal mixing

$$M_H(T) = \frac{\partial T}{\partial t} + u \frac{\partial T}{\partial x} + v \frac{\partial T}{\partial y} + w \frac{\partial T}{\partial z} - \delta_z(\kappa \delta_z T) \quad (4)$$

It is a good representation in the deep ocean where high-frequency noises are small. All estimates are based on the decadal mean outputs. The unit of each term is ‰ s<sup>-1</sup> for  $\delta^{18}\text{O}_w$  analysis and °C s<sup>-1</sup> for temperature analysis. A detailed description of the offline scheme of each term is in Zhang (37), Appendix C.

The results of the tracer budget analyses performed on  $\delta^{18}\text{O}_w$  and temperature are shown in Fig. 5 and discussed in the main text. In Fig. 5 *F*, the increase of warming by horizontal mixing starting from 17 ka is associated with the increase of along-isopycnal diffusion of heat, since eddy activity at the 3100-m depth is ignorable. At the LGM, the deep water temperature is almost uniform (Fig. 4*B*) and there is little along-isopycnal diffusion of heat. After 17 ka, the northern North Atlantic warms more than in the tropics (Fig. 4*F*, the tilted warming) and increases the along-isopycnal temperature gradient, resulting in the increase of along-isopycnal diffusion of heat.

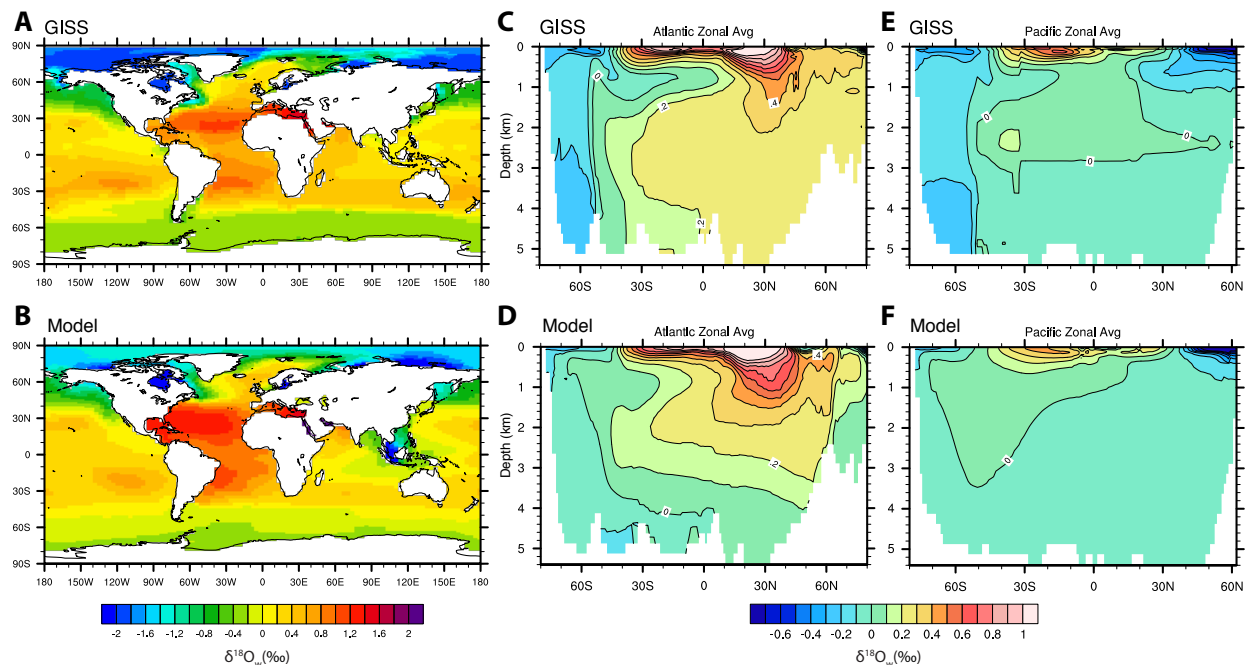


**Figure S1.** Validation of the oxygen isotope module with modern climate conditions. Annual-mean gridded GISS-O18 observational  $\delta^{18}\text{O}_w$  (12, 13) are shown at sea surface (A) and zonally averaged in the Atlantic (C) and Pacific (E) basins, and are compared with the  $\delta^{18}\text{O}_w$  simulated in iMODspin (B, D, and F). The model results use average of the last 50 y of the 4,000-y iMODspin simulation.

## T-S Diagram

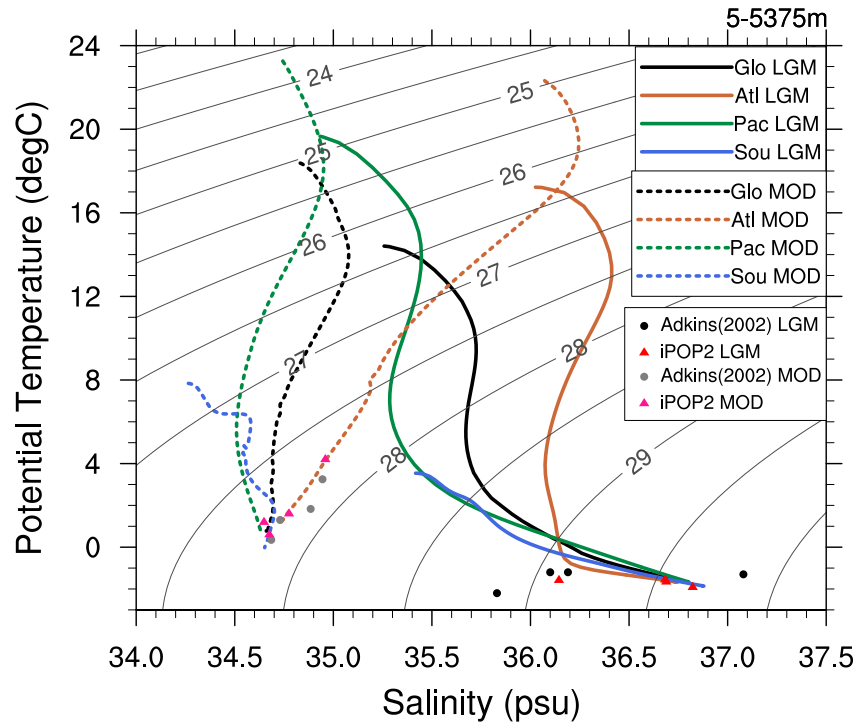


**Figure S2.** Temperature-salinity (T-S) diagram with full-depth profiles averaged over the major ocean basins for the iLGMspin (solid) and iMODspin (dashed) experiments. Deep ocean T-S relations are also plotted for modern observations (gray dots), LGM reconstructions (black dots) (17), iMODspin (pink triangles), and iLGMspin (red triangles) at four Ocean Drilling Program sites: site 981 (Feni Drift; 55° N, 15° W, 2,814 m), site 1063 (Bermuda Rise; 34° N, 58° W, 4,584 m), site 1093 (Shona Rise; 50° S, 6° E, 3,626 m), and site 1123 (Chatham Rise; 42° S, 171° W, 3,290 m). Contours indicate potential density ( $\sigma_\theta$ ) values in units of  $\text{kg m}^{-3}$ .

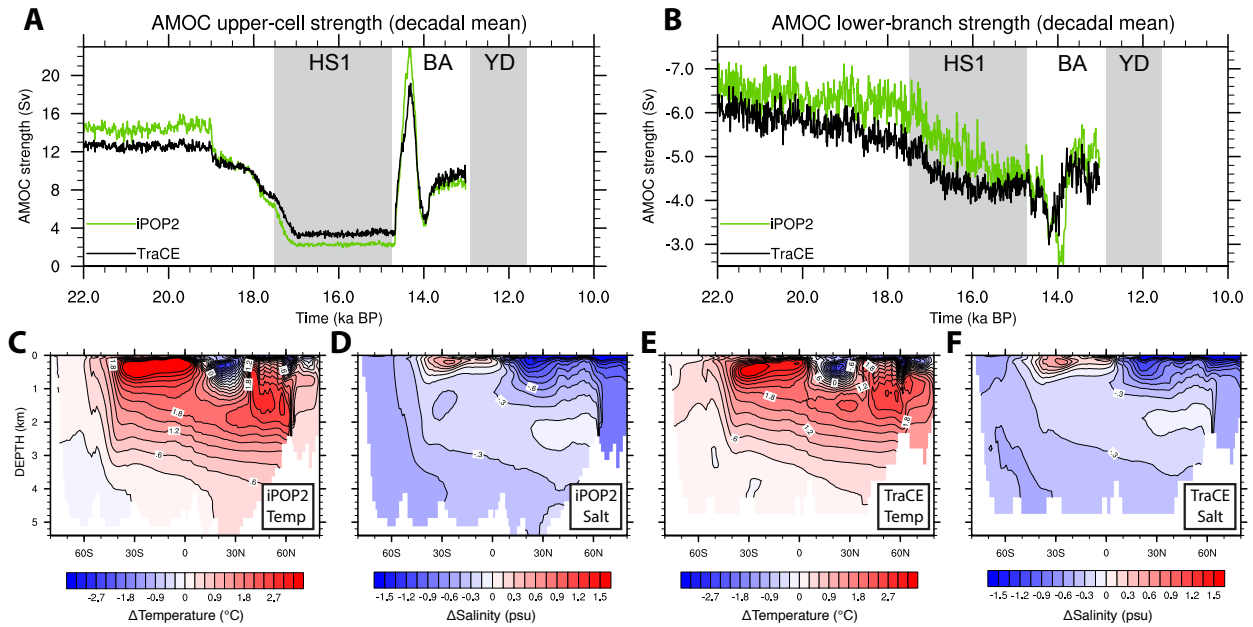


**Figure S3.** Changes of AMOC strength (*A* and *B*) as well as Atlantic zonally averaged temperature and salinity (*C–F*) in the iPOP2-TRACE and TRACE21 simulations. (*A*) iPOP2-TRACE (green) AMOC strength of the upper cell compare with that of TRACE21 (black). (*B*) Same as *A*, but for the AMOC abyssal cell, which is defined as the minimum AMOC transport in the Southern Atlantic below 2,000 m. Negative values indicate counterclockwise circulation. (*C* and *D*) Temperature and salinity changes between HS1 at 16 ka and glacial at 19 ka in iPOP2-TRACE. (*E* and *F*) Same as *C* and *D*, but for TRACE21. The AMOC strength evolution as well as changes of both temperature and salinity fields in iPOP2-TRACE highly reproduce those in TRACE21, confirming that iPOP2-TRACE experiences similar dynamical evolution as TRACE21 does.

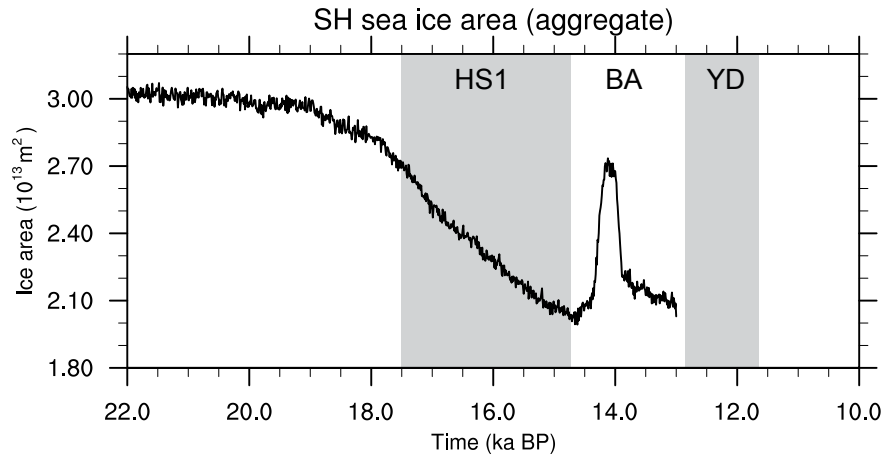


**Figure S4.** Time series of aggregated sea ice area in the Southern Ocean in iPOP2-TRACE. Sea ice starts to retreat at 19.0 ka due to initial warming in the Southern Hemisphere, promoting air-sea gas exchange and contributing to the initial rise of the atmospheric CO<sub>2</sub>. By the end of HS1, the Southern Ocean has significantly reduced by 33% compared with the LGM.

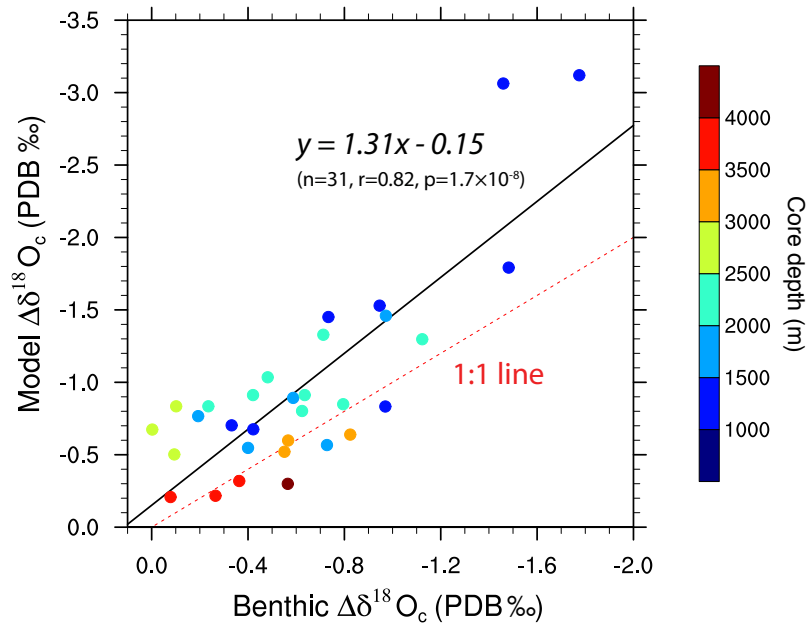


**Figure S5.** Correlation between measured Atlantic benthic  $\delta^{18}\text{O}_c$  changes [between late HS1 (16.3–14.8 ka mean) and glacial (20.5–19.0 ka mean) periods] and model outputs from grid cells closest to core locations. Colors represent core depths. The geographic locations of the 31 Atlantic cores are shown in Fig. 3 and listed in Table S2. The black line represents linear regression (with correlation of 0.82) and the red dashed line is the 1:1 line.

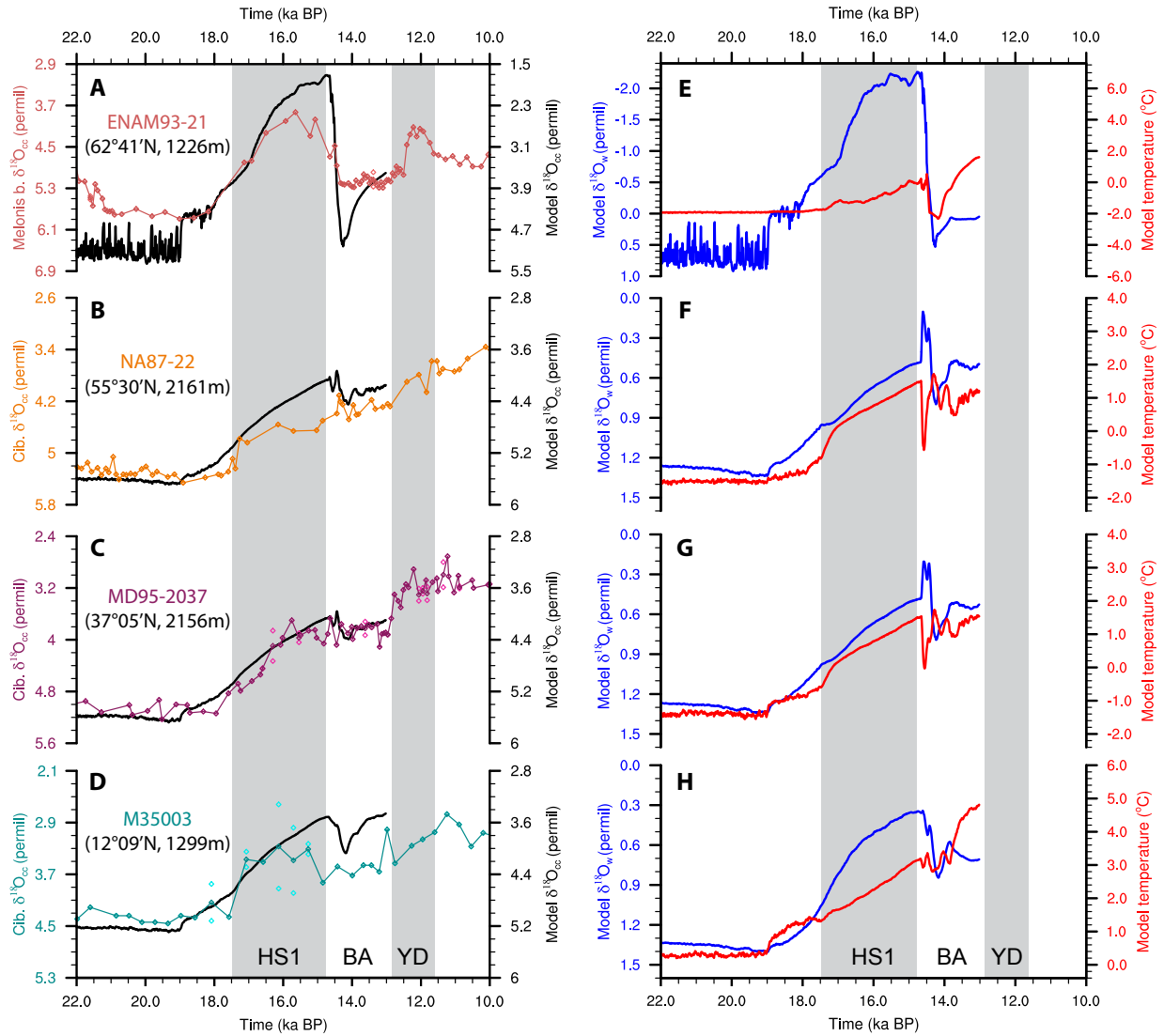


**Figure S6.** Model-data comparison for middepth  $\delta^{18}O_e$  records. (A–D) Norwegian Sea and North Atlantic benthic  $\delta^{18}O_e$  records (38) from the 1,000–2,200 m depth range, and model  $\delta^{18}O_e$  (black) at the corresponding sites. Complete references for the isotopic measurements and age models of the  $\delta^{18}O_e$  records are summarized in Waelbroeck et al. (38). (E–H) Simulated water  $\delta^{18}O_w$  (blue) and temperature (red) at each site as indicated on the left panel.

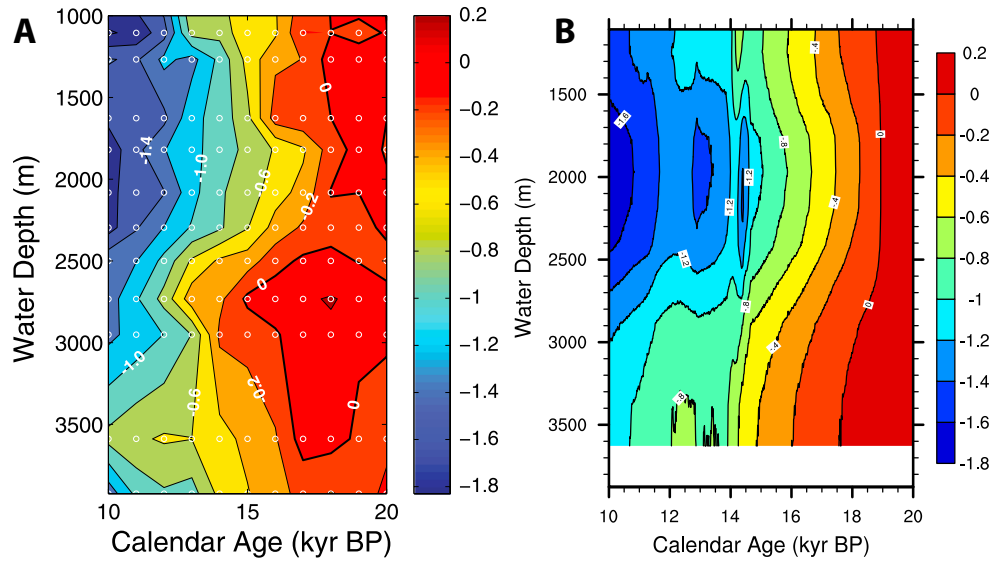


**Figure S7.** Model-data comparisons for  $\delta^{18}\text{O}_c$  transect near the Brazil Margin in the South Atlantic. (A) Hovmöller diagram of  $\delta^{18}\text{O}_c$  anomalies for the 10-20 kyr B.P. time interval. Anomalies are the stable isotope value at each water depth minus the mean LGM value (19–23 kyr B.P.) at that depth. Reprinted with permission from ref. 35. (B) Model Hovmöller diagram at the same location as in A. The model results reproduce the proxies both in pattern and magnitude. Both show upper depths  $\delta^{18}\text{O}_c$  started to decrease much earlier than lower depths.

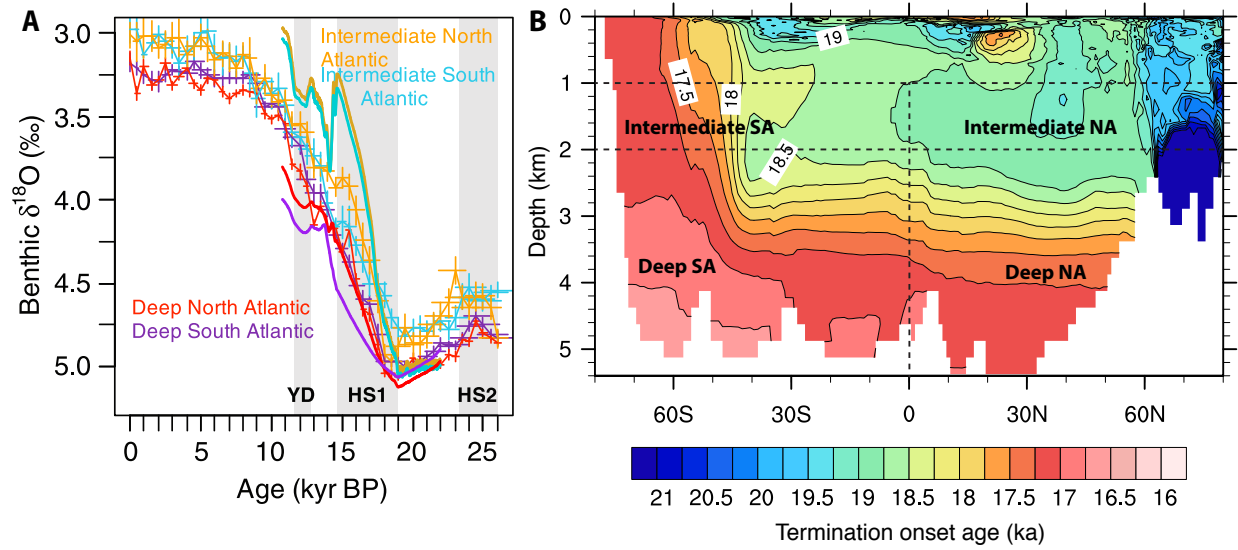


**Figure S8.**  $\delta^{18}\text{O}_c$  indicated termination onset age. (A) Model  $\delta^{18}\text{O}_c$  compares with Atlantic regional benthic  $\delta^{18}\text{O}_c$  stacks (36) for the last deglaciation. The lines with error bars are the stacks at four regions, indicated by different colors and noted in the figure. Reprinted with permission from ref. 36. Error bars show the 95% age uncertainty and  $\pm 1$  standard error for stacked  $\delta^{18}\text{O}_c$  values. Solid lines are the model results, sampling at the same core cites as the stacks do. (B) Model simulated age (kyr B.P.) of the termination onset, which is defined as the first  $\delta^{18}\text{O}_c$  point that is at least 0.1‰ lighter than the maximum  $\delta^{18}\text{O}_c$  value (36). Dash lines indicate the four regions as defined in A.

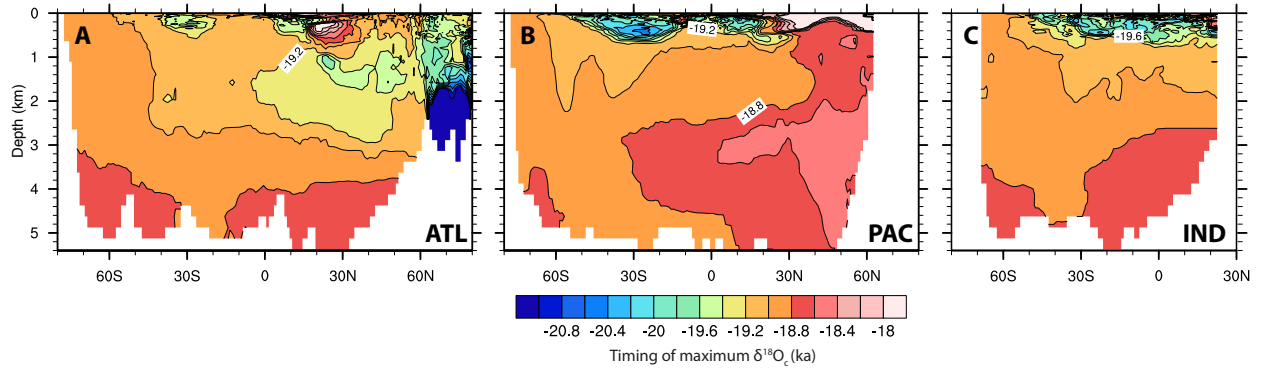


**Figure S9.** Zonally averaged timing of maximum  $\delta^{18}\text{O}_c$  at (A) Atlantic, (B) Pacific, and (C) Indian Ocean basins. Maximum values are generally reached first at upper ocean layers, then at intermediate and deep ocean. The deep North Pacific is found to be the region which reached its local maximum  $\delta^{18}\text{O}_c$  latest (after 18.6 ka).

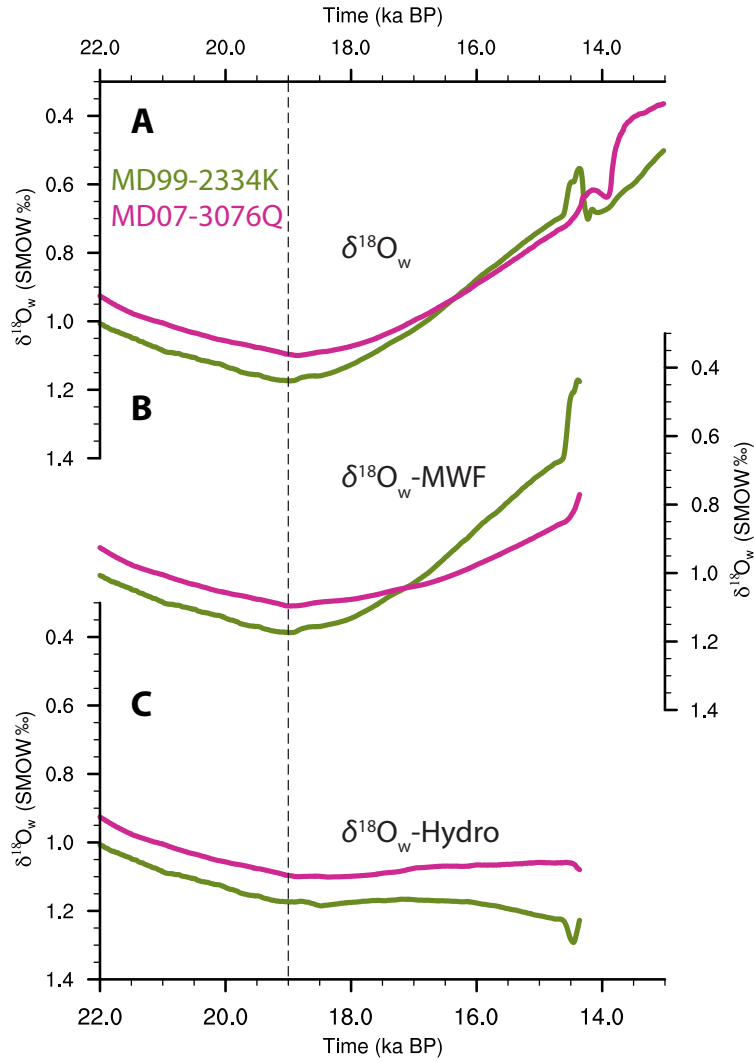


**Figure S10.** Standard  $\delta^{18}\text{O}_w$  and two sensitivity tracers at the two deep Atlantic core sites. (A) Simulated  $\delta^{18}\text{O}_w$  at Iberian Margin (MD99-2334K, green) and Southern Ocean (MD07-3076Q, pink) sites, replot of Fig. 1F. (B) Sensitivity tracer  $\delta^{18}\text{O}$ -MWF, which is forced by transient meltwater  $\delta^{18}\text{O}$  forcing but with surface hydrographic forcing fixed at the 19-ka level. (C) Sensitivity tracer  $\delta^{18}\text{O}$ -Hydro, which is forced by transient surface hydrographic forcing but no meltwater  $\delta^{18}\text{O}$  forcing. Details about  $\delta^{18}\text{O}$ -MWF and  $\delta^{18}\text{O}$ -Hydro can be found in Method S7.

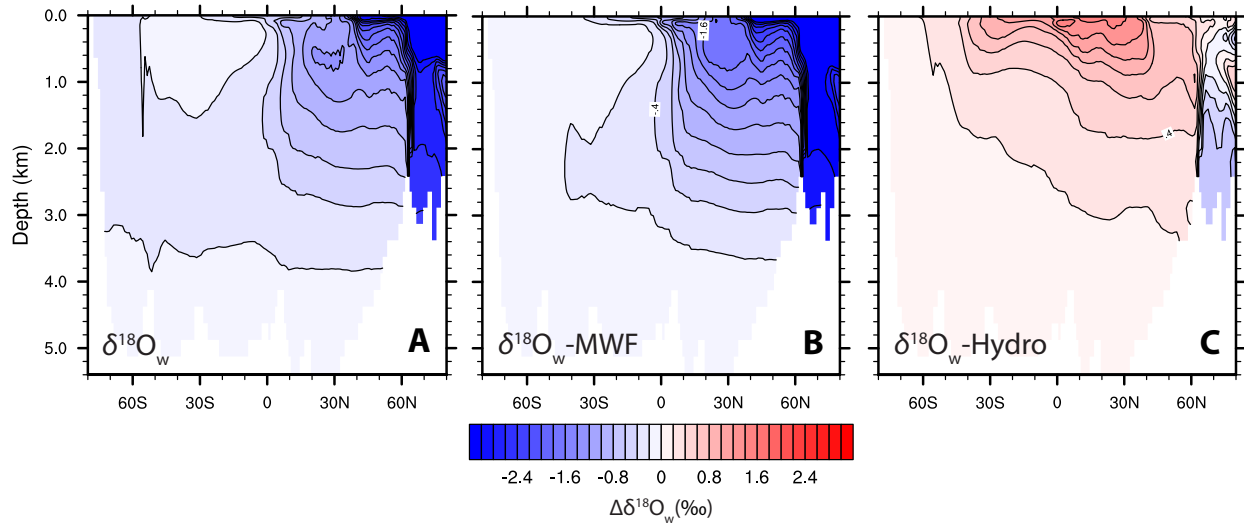


**Figure S11.** Atlantic zonally averaged  $\delta^{18}\text{O}_w$  changes for the stand  $\delta^{18}\text{O}_w$  (A) and two sensitivity tracers  $\delta^{18}\text{O}_w$ -MWF (B) and  $\delta^{18}\text{O}_w$ -Hydro (C) in the iPOP2-TRACE simulation. Refer to Method S7 for tracer details. All changes were computed as the differences between 16 ka and 19 ka.

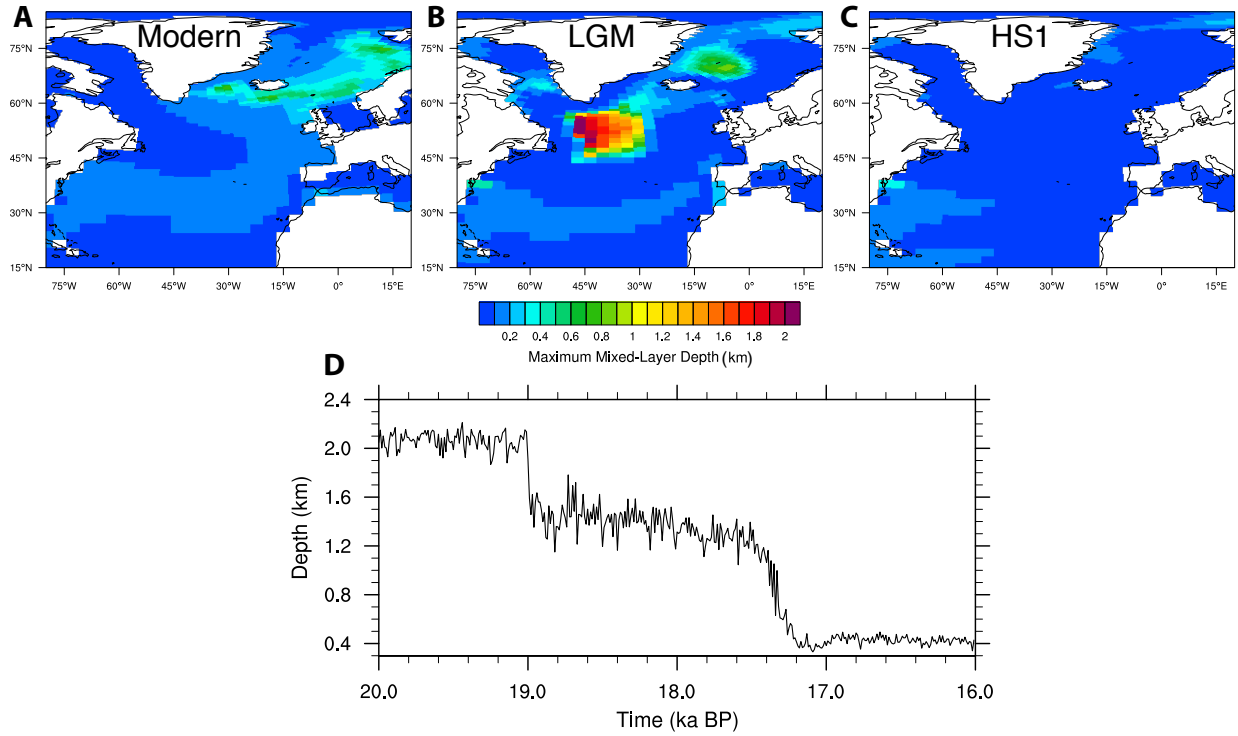


**Figure S12.** Winter season (December, January, and February) maximum mixed-layer depth, which indicates the deep-water formation regions, are plotted for the modern (*A*), LGM at 19 ka (*B*), and late HS1 at 16 ka (*C*). (*D*) Time series of winter season maximum mixed-layer depth in the North Atlantic for the 20–16 ka BP time interval. Two sudden drops are found at 19.0 and 17.3 ka.

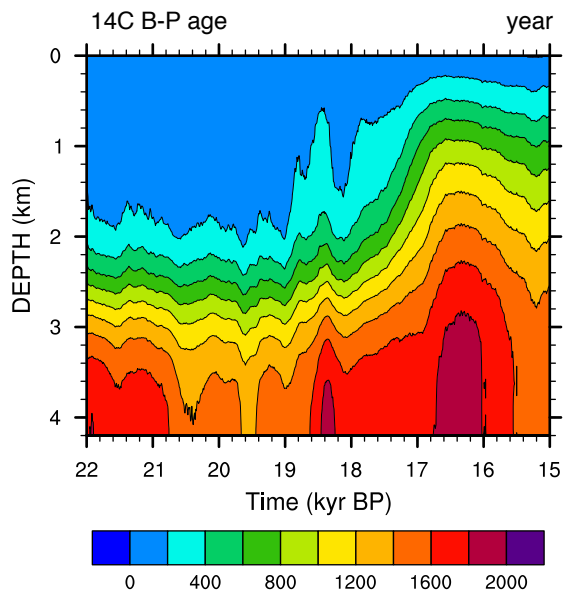


**Figure S13.** Hovmöller diagram of area averaged  $^{14}\text{C}$  B-P age offset in the northern NA (>30°N), which is the same region used in plotting Fig. 5 *A* and *E*. Before 19 ka, the upper 2,000 m water is well mixed and the B-P age is within 200 years. At 19 ka, in response to the sudden shoaling of the deep convection, the 200-year contour also shoals to 1,000 m depth.

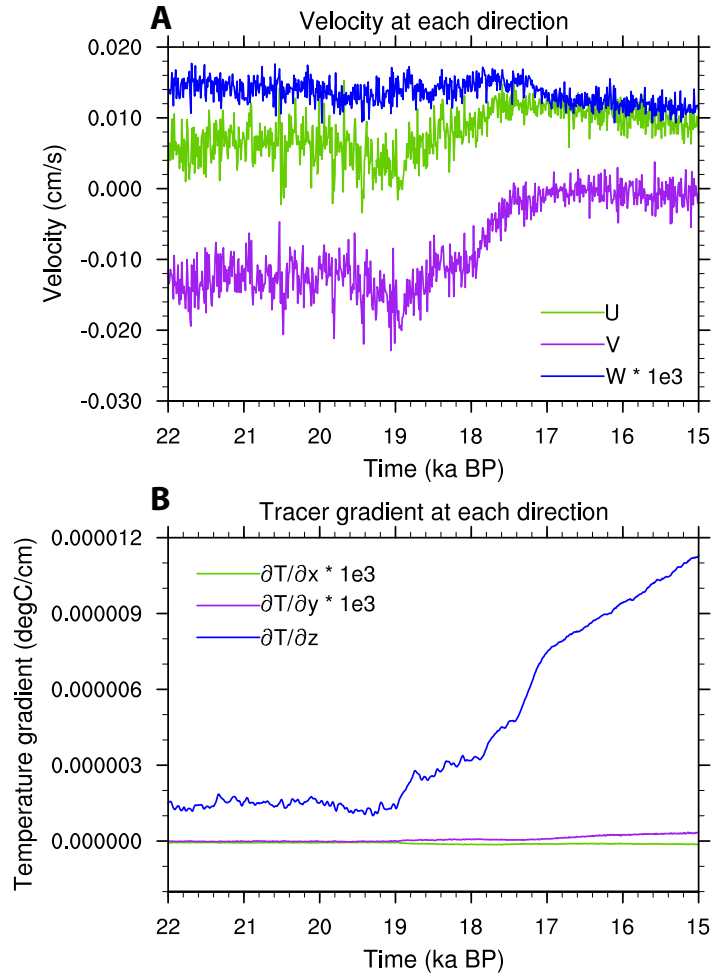


**Figure S14.** Breakdown of the three mean advection terms of Fig. 5E into (A) mean velocities and (B) temperature gradients. Zonal, meridional, and vertical directions are represented by green, purple and blue. The vertical velocity in A and two horizontal temperature gradients in B are enlarged by 1,000 times in order for comparison. The vertical velocity does not change much as the horizontal velocities do after 19 ka. Instead, the vertical temperature gradient has a marked increase.

Table S1

Locations and amounts of meltwater forcing in each period during the last deglaciation used in TRACE21 (14, 15). NH, Northern Hemisphere; SH, Southern Hemisphere. Each location is specified as: North Atlantic, 50° N–70° N, 80° W–20° E; Gulf of Mexico, 15° N–33° N, 255° E–280° E; Mackenzie River, 65° N–75° N, 210° E–240° E; Nordic Sea, 55° N–75° N, 15° W–30° E; St. Lawrence River, 38° N–60° N, 270° E–310° E; Ross Sea, 60° S–80° S, 140° E–220° E; Weddell Sea, 60° S–80° S, 70° W–30° E.

Age (ka)	NH amount (m/kyr)	NH location	SH amount (m/kyr)	SH location
22.0–19.0	/	/	/	/
19.0–18.4	3	North Atlantic	/	/
18.4–17.5	Ramping 3 to 5	North Atlantic	/	/
	Ramping 0 to 5	Gulf of Mexico	/	/
17.5–17.0	Ramping 5 to 15	North Atlantic	/	/
	5	Gulf of Mexico	/	/
17.0–14.67	15	North Atlantic	/	/
14.67–14.35	/	/	/	/
14.35–14.1	Ramping 0 to 10	Mackenzie River	Ramping 0 to 30	Ross Sea
	Ramping 0 to 10	Gulf of Mexico	Ramping 0 to 30	Weddell Sea
14.1–13.85	Ramping 10 to 0	Mackenzie River	Ramping 30 to 0	Ross Sea
	Ramping 10 to 0	Gulf of Mexico	Ramping 30 to 0	Weddell Sea
13.87–13.0	1	Nordic Sea	5	Ross Sea
13.87–13.4	4	Gulf of Mexico	/	
13.4–13.0	2.4	Gulf of Mexico	/	
	1.6	St. Lawrence River	/	

Table S2

List of 31 Atlantic benthic  $\delta^{18}\text{O}_c$  cores at intermediate and deep depths (below 1,000 m) used in Fig. 3. We collected published, high-resolution cores, which have independently-dated radiocarbon dates and multiple data points (except for GIK13289-2 and EW9209-1JPC) falling in each 1,500-y window (glacial window, 20.5–19.0 ka; late HS1 window, 16.3–14.8 ka).

Core	Latitude	Longitude	Depth (m)	Benthic species	# of glacial points	# of HS1 points
MD95-2010 (39)	66.68	-4.57	1226	<i>Cibicides sp.</i>	18	16
ENAM93-21 (40, 41)	62.74	-4	1020	<i>Melonis barleanum</i>	4	4
EW9302-24GGC (42)	61.76	-21.67	1629	<i>C. wuellerstorfi</i>	2	2
NA87-22 (31, 32)	55.5	-14.7	2161	<i>Cibicides sp.</i>	8	4
KN166-14-JPC-13 (43)	53.06	-31.53	3082	<i>C. wuellerstorfi</i>	7	2
EW9302-2JPC (44)	48.8	-45.08	1251	<i>C. wuellerstorfi</i>	2	3
MD99-2334K (45, 46)	37.8	-10.17	3146	<i>P. wuellerstorfi</i> , <i>G. affinis</i>	7	7
MD95-2037 (33, 34)	37.09	-32.03	2159	<i>Cibicides sp.</i>	6	10
MD99-2339 (47)	35.89	-7.53	1177	<i>Cibicides sp.</i> , <i>Uvigerina sp.</i>	17	13
GeoB7920-2 (48, 49)	20.75	-18.58	2278	<i>C. wuellerstorfi</i>	2	3
GIK13289-2 (50)	18.07	-18.01	2485	<i>C. wuellerstorfi</i>	2	1
GeoB9508-5 (51)	14.5	-17.95	2384	<i>Cibicides sp.</i>	6	23
GeoB9526-4	12.44	-18.06	3223	<i>C. wuellerstorfi</i>	2	9
M35003-4 (52–54)	12.09	-61.24	1299	<i>C. wuellerstorfi</i>	4	4
EW9209-1JPC (55, 56)	5.91	-44.2	4056	<i>C. wuellerstorfi</i>	2	1
MD03-2707 (57)	2.50	9.395	1295	<i>C. pachyderma</i>	16	8
GeoB1711 (58, 59)	-23.32	12.38	1967	<i>C. wuellerstorfi</i>	6	5
KNR159-5-90GGC (35, 60)	-27.35	-46.63	1105	<i>Cibicides sp.</i> , <i>Planulina sp.</i>	5	5
KNR159-5-36GGC (60, 61)	-27.27	-46.47	1268	<i>Cibicides sp.</i> , <i>Planulina sp.</i>	5	8
KNR159-5-17JPC (62)	-27.7	-46.49	1627	<i>Cibicides sp.</i>	3	2
KNR159-5-78GGC (62)	-27.48	-46.33	1829	<i>Cibicides sp.</i>	13	4
KNR159-5-33GGC (62)	-27.56	-46.19	2082	<i>Cibicides sp.</i>	5	3
KNR159-5-42JPC (60, 63)	-27.76	-46.63	2296	<i>Cibicides sp.</i> , <i>Planulina sp.</i>	5	11
KNR159-5-73GGC (42)	-27.89	-46.04	2397	<i>C. wuellerstorfi</i>	2	3
KNR159-5-30GGC (62)	-28.13	-46.07	2500	<i>Cibicides sp.</i>	2	2
KNR159-5-63GGC (35)	-27.7	-46.5	2732	<i>C. wuellerstorfi</i>	2	2
KNR159-5-20JPC (35)	-28.64	-45.54	2951	<i>C. wuellerstorfi</i>	5	2
KNR159-5-125GGC (63)	-29.53	-45.08	3589	<i>Cibicides sp.</i>	5	2
KNR159-5-22GGC (63)	-29.78	-43.58	3924	<i>Cibicides sp.</i>	2	4
GeoB1720-2 (64)	-29	13.84	1997	<i>C. wuellerstorfi</i>	2	2

MD07-3076Q (38, 65)	-44.07	-14.21	3770	<i>C. kullenbergi</i>	6	6
---------------------	--------	--------	------	-----------------------	---	---

## References

1. Danabasoglu G, et al. (2012) The CCSM4 Ocean Component. *J Clim* 25(5):1361–1389.
2. Hurrell JW, et al. (2013) The Community Earth System Model: A framework for collaborative research. *Bull Am Meteorol Soc* 94(9):1339–1360.
3. Griffies SM (1998) The Gent–McWilliams skew flux. *J Phys Oceanogr* 28(5):831–841.
4. Large WG, McWilliams JC, Doney SC (1994) Oceanic vertical mixing: A review and a model with a nonlocal boundary layer parameterization. *Rev Geophys* 32(4):363.
5. Danabasoglu G, et al. (2006) Diurnal coupling in the tropical oceans of CCSM3. *J Clim* 19(11):2347–2365.
6. Yeager SG, Shields CA, Large WG, Hack JJ (2006) The Low-Resolution CCSM3. *J Clim* 19(11):2545–2566.
7. Otto-Bliesner BL, et al. (2007) Last Glacial Maximum ocean thermohaline circulation: PMIP2 model intercomparisons and data constraints. *Geophys Res Lett* 34(12):L12706.
8. Brady EC, Otto-Bliesner BL, Kay JE, Rosenbloom N (2013) Sensitivity to Glacial Forcing in the CCSM4. *J Clim* 26(6):1901–1925.
9. Schmidt GA (1999) Forward modeling of carbonate proxy data from planktonic foraminifera using oxygen isotope tracers in a global ocean model. *Paleoceanography* 14(4):482–497.
10. Griffies SM, et al. (2012) Datasets and protocol for the CLIVAR WGOMD Coordinated Ocean-sea ice Reference Experiments (COREs). World Climate Research Programme, Report No. 21/2012.
11. Yeager S, Karspeck A, Danabasoglu G, Tribbia J, Teng H (2012) A Decadal Prediction Case Study: Late Twentieth-Century North Atlantic Ocean Heat Content. *J Clim* 25(15):5173–5189.
12. Schmidt G, Bigg GR, Rohling EJ (1999) Global seawater oxygen-18 database - v1.21. Available at: <http://data.giss.nasa.gov/o18data/>.
13. LeGrande AN, Schmidt G a. (2006) Global gridded data set of the oxygen isotopic composition in seawater. *Geophys Res Lett* 33(12):L12604.
14. Liu Z, et al. (2009) Transient simulation of last deglaciation with a new mechanism for Bølling-Allerød warming. *Science* 325(5938):310–314.
15. He F (2011) Simulating transient climate evolution of the last deglaciation with CCSM3. PhD Dissertation (University of Wisconsin–Madison).
16. Tziperman E, Toggweiler JR, Bryan K, Feliks Y (1994) Instability of the thermohaline circulation with respect to mixed boundary conditions: Is it really a problem for realistic models? *J Phys Oceanogr* 24(2):217–232.
17. Adkins JF, McIntyre K, Schrag DP (2002) The salinity, temperature, and  $\delta^{18}\text{O}$  of the glacial deep ocean. *Science* 298(5599):1769–1773.
18. Liu Z, et al. (2014) Chinese cave records and the East Asia Summer Monsoon. *Quat Sci Rev* 83:115–128.
19. Sima A, Paul A, Schulz M, Oerlemans J (2006) Modeling the oxygen-isotopic composition of the North American Ice Sheet and its effect on the isotopic composition of the ocean during the last glacial cycle. *Geophys Res Lett* 33(15):L15706.
20. Stenni B, et al. (2011) Expression of the bipolar see-saw in Antarctic climate records during the last deglaciation. *Nat Geosci* 4(1):46–49.
21. Steig EJ, et al. (1998) Change in climate, ocean and ice-sheet conditions in the Ross

- embayment, Antarctica, at 6 ka. *Ann Glaciol* 27:305–310.
22. Orr J, Najjar R, Sabine C, Joos F (2000) *Abiotic-HOWTO* (Gif-sur-Yvette, France).
  23. Jahn A, et al. (2015) Carbon isotopes in the ocean model of the Community Earth System Model (CESM1). *Geosci Model Dev* 8(8):2419–2434.
  24. Fiadeiro ME (1982) Three-dimensional modeling of tracers in the deep Pacific Ocean II: radiocarbon and the circulation. *J Mar Res* 40:537–550.
  25. Joos F, Spahni R (2008) Rates of change in natural and anthropogenic radiative forcing over the past 20,000 years. *Proc Natl Acad Sci* 105(5):1425–1430.
  26. Reimer PJ, et al. (2009) INTCAL09 and MARINE09 radiocarbon age calibration curves, 0–50,000 years cal BP. *Radiocarbon* 51(4):1111–1150.
  27. Marchitto TM, et al. (2014) Improved oxygen isotope temperature calibrations for cosmopolitan benthic foraminifera. *Geochim Cosmochim Acta* 130:1–11.
  28. Hut G (1987) *Consultants' group meeting on stable isotope reference samples for geochemical and hydrological investigations* (Vienna).
  29. Shackleton NJ (1974) Attainment of isotopic equilibrium between ocean water and the benthonic foraminifera genus *Uvigerina*: Isotopic changes in the ocean during the last glacial. *Colloq Int CNRS* 219:203–209.
  30. Duplessy J-C, et al. (1984)  $^{13}\text{C}$  Record of benthic foraminifera in the last interglacial ocean: Implications for the carbon cycle and the global deep water circulation. *Quat Res* 21(2):225–243.
  31. Vidal L, et al. (1997) Evidence for changes in the North Atlantic Deep Water linked to meltwater surges during the Heinrich events. *Earth Planet Sci Lett* 146:13–27.
  32. Waelbroeck C, et al. (2001) The timing of the last deglaciation in North Atlantic climate records. *Nature* 412(6848):724–7.
  33. Labeyrie L, Waelbroeck C, Cortijo E, Michel E, Duplessy J-C (2005) Changes in deep water hydrology during the Last Deglaciation. *Comptes Rendus Geosci* 337(10–11):919–927.
  34. Gherardi J -M., et al. (2009) Glacial-interglacial circulation changes inferred from  $^{231}\text{Pa}/^{230}\text{Th}$  sedimentary record in the North Atlantic region. *Paleoceanography* 24(2):PA2204.
  35. Lund DC, Tessin a C, Hoffman JL, Schmittner A (2015) Southwest Atlantic water mass evolution during the last deglaciation. *Paleoceanography* 30(5):477–494.
  36. Stern J V., Lisiecki LE (2014) Termination 1 timing in radiocarbon-dated regional benthic  $\delta^{18}\text{O}$  stacks. *Paleoceanography* 29(12):1127–1142.
  37. Zhang J (2016) Understanding the deglacial evolution of deep Atlantic water masses in an isotope-enabled ocean model. PhD Dissertation (University of Wisconsin–Madison).
  38. Waelbroeck C, et al. (2011) The timing of deglacial circulation changes in the Atlantic. *Paleoceanography* 26(3):PA3213.
  39. Dokken TM, Jansen E (1999) Rapid changes in the mechanism of ocean convection during the last glacial period. *Nature* 401:458–461.
  40. Rasmussen TL, Thomsen E, Labeyrie L, van Weering TCE (1996) Circulation changes in the Faroe-Shetland Channel correlating with cold events during the last glacial period (58–10ka). *Geology* 24(10):937–940.
  41. Rasmussen TL, Thomsen E, van Weering TCE (1998) Cyclic sedimentation on the Faeroe Drift 53–10 ka BP related to climatic variations. *Geological Processes on Continental Margins: Sedimentation, Mass-Wasting and Stability*, eds Stoker MS, Evans D, Cramp A

- (Geological Society Special Publications, London), pp 255–267.
42. Oppo DW, Curry WB, McManus JF (2015) What do benthic  $\delta^{13}\text{C}$  and  $\delta^{18}\text{O}$  data tell us about Atlantic circulation during Heinrich Stadial 1? *Paleoceanography* 30(4):353–368.
  43. Hodell D a., Evans HF, Channell JET, Curtis JH (2010) Phase relationships of North Atlantic ice-rafted debris and surface-deep climate proxies during the last glacial period. *Quat Sci Rev* 29(27–28):3875–3886.
  44. Rasmussen TL, Oppo DW, Thomsen E, Lehman SJ (2003) Deep sea records from the southeast Labrador Sea: Ocean circulation changes and ice-rafting events during the last 160,000 years. *Paleoceanography* 18(1):1018.
  45. Skinner LC, Shackleton NJ, Elderfield H (2003) Millennial-scale variability of deep-water temperature and  $\delta^{18}\text{O}_{\text{dw}}$  indicating deep-water source variations in the Northeast Atlantic, 0–34 cal. ka BP. *Geochem Geophys Geosyst* 4(12):n/a-n/a.
  46. Skinner LC, Shackleton NJ (2004) Rapid transient changes in northeast Atlantic deep water ventilation age across Termination I. *Paleoceanography* 19(2):PA2005.
  47. Voelker AHL, et al. (2006) Mediterranean outflow strengthening during northern hemisphere coolings: A salt source for the glacial Atlantic? *Earth Planet Sci Lett* 245(1–2):39–55.
  48. Tjallingii R, et al. (2008) Coherent high- and low-latitude control of the northwest African hydrological balance. *Nat Geosci* 1(10):670–675.
  49. Collins JA, et al. (2011) Interhemispheric symmetry of the tropical African rainbelt over the past 23,000 years. *Nat Geosci* 4(1):42–45.
  50. Sarnthein M, et al. (1994) Changes in East Atlantic Deepwater Circulation over the last 30,000 years: Eight time slice reconstructions. *Paleoceanography* 9(2):209–267.
  51. Mulitza S, et al. (2008) Sahel megadroughts triggered by glacial slowdowns of Atlantic meridional overturning. *Paleoceanography* 23(4):PA4206.
  52. Rühlemann C, Mulitza S, Müller PJ, Wefer G, Zahn R (1999) Warming of the tropical Atlantic Ocean and slowdown of thermohaline circulation during the last deglaciation. *Nature* 402(6761):511–514.
  53. Rühlemann C, et al. (2004) Intermediate depth warming in the tropical Atlantic related to weakened thermohaline circulation: Combining paleoclimate data and modeling results for the last deglaciation. *Paleoceanography* 19(1):PA1025.
  54. Zahn R, Stüber A (2002) Suborbital intermediate water variability inferred from paired benthic foraminiferal Cd/Ca and  $\delta^{13}\text{C}$  in the tropical West Atlantic and linking with North Atlantic climates. *Earth Planet Sci Lett* 200(1–2):191–205.
  55. Curry WB, Oppo DW (1997) Synchronous, high-frequency oscillations in tropical sea surface temperatures and North Atlantic Deep Water production during the last glacial cycle. *Paleoceanography* 12(1):1–14.
  56. Ostermann DR, Curry WB (2000) Calibration of stable isotopic data: An enriched  $\delta^{18}\text{O}$  standard used for source gas mixing detection and correction. *Paleoceanography* 15(3):353–360.
  57. Weldeab S, Friedrich T, Timmermann A, Schneider RR (2016) Strong middepth warming and weak radiocarbon imprints in the equatorial Atlantic during Heinrich 1 and Younger Dryas. *Paleoceanography* 31:1–13.
  58. Little MG, et al. (1997) Rapid palaeoceanographic changes in the Benguela Upwelling System for the last 160,000 years as indicated by abundances of planktonic foraminifera. *Palaeogeogr Palaeoclimatol Palaeoecol* 130(1–4):135–161.

59. Vidal L, et al. (1999) Link between the North and South Atlantic during the Heinrich events of the last glacial period. *Clim Dyn* 15(12):909–919.
60. Curry WB, Oppo DW (2005) Glacial water mass geometry and the distribution of  $\delta^{13}\text{C}$  of  $\Sigma\text{CO}_2$  in the western Atlantic Ocean. *Paleoceanography* 20(1):PA1017.
61. Sortor RN, Lund DC (2011) No evidence for a deglacial intermediate water  $\Delta^{14}\text{C}$  anomaly in the SW Atlantic. *Earth Planet Sci Lett* 310(1–2):65–72.
62. Tessin a. C, Lund DC (2013) Isotopically depleted carbon in the mid-depth South Atlantic during the last deglaciation. *Paleoceanography* 28(November 2012):296–306.
63. Hoffman JL, Lund DC (2012) Refining the stable isotope budget for Antarctic Bottom Water: New foraminiferal data from the abyssal southwest Atlantic. *Paleoceanography* 27(1):PA1213.
64. Dickson AJ, et al. (2009) Oceanic forcing of the Marine Isotope Stage 11 interglacial. *Nat Geosci* 2(6):428–433.
65. Skinner LC, Fallon S, Waelbroeck C, Michel E, Barker S (2010) Ventilation of the deep Southern Ocean and deglacial  $\text{CO}_2$  rise. *Science* 328(5982):1147–1151.